HHS Public Access

Author manuscript

Mol Pharm. Author manuscript; available in PMC 2024 January 21.

Published in final edited form as:

Mol Pharm. 2023 March 06; 20(3): 1670–1680. doi:10.1021/acs.molpharmaceut.2c00880.

Targeting Intratibial Osteosarcoma Using Water-Soluble Copolymers Conjugated to Collagen Hybridizing Peptides

Nithya Subrahmanyam,
Department of Molecular Pharmaceutics, University of Utah, Salt Lake City, Utah 84112, United States; Utah Center for Nanomedicine, University of Utah, Salt Lake City, Utah 84112, United States

Bhuvanesh Yathavan,
Department of Molecular Pharmaceutics, University of Utah, Salt Lake City, Utah 84112, United States; Utah Center for Nanomedicine, University of Utah, Salt Lake City, Utah 84112, United States

S. Michael Yu,
Department of Molecular Pharmaceutics, University of Utah, Salt Lake City, Utah 84112, United States; Department of Biomedical Engineering, University of Utah, Salt Lake City, Utah 84112, United States

Hamidreza Ghandehari
Department of Molecular Pharmaceutics, University of Utah, Salt Lake City, Utah 84112, United States; Utah Center for Nanomedicine and Department of Biomedical Engineering, University of Utah, Salt Lake City, Utah 84112, United States

Abstract

Osteosarcoma (OS) is the most common form of primary malignant bone cancer in adolescents. Over the years, OS prognosis has greatly improved due to adjuvant and neoadjuvant (preoperative) chemotherapeutic treatment, increasing the chances of successful surgery and reducing the need for limb amputation. However, chemotherapeutic treatment to treat OS is limited by off-target toxicities and requires improved localization at the tumor site. Collagen, the main constituent of bone tissue, is extensively degraded and remodeled in OS, leading to an increased availability of denatured (monomeric) collagen. Collagen hybridizing peptides (CHPs) comprise a class of peptides rationally designed to selectively bind to denatured collagen. In this work, we have conjugated CHPs as targeting moieties to water-soluble *N*-(2-hydroxypropyl)methacrylamide (HPMA) copolymers to target OS tumors. We demonstrated increased accumulation of collagen-

Corresponding Author: **Hamidreza Ghandehari** – *Department of Molecular Pharmaceutics, University of Utah, Salt Lake City, Utah 84112, United States; Utah Center for Nanomedicine and Department of Biomedical Engineering, University of Utah, Salt Lake City, Utah 84112, United States;* hamid.ghandehari@utah.edu.

Supporting Information

The Supporting Information is available free of charge at https://pubs.acs.org/doi/10.1021/acs.molpharmaceut.2c00880.
Fluorescence images of in vivo mice experiments, ex vivo organ and bone tissue analyses, as well as Pearson correlation coefficient *r* values for accumulation with respect to bone morphometric parameters extracted from μ-CT analysis (PDF)

Complete contact information is available at: https://pubs.acs.org/10.1021/acs.molpharmaceut.2c00880

The authors declare no competing financial interest.

targeted HPMA copolymer–CHP conjugates compared to nontargeted HPMA copolymers, as well as increased retention compared to both nontargeted copolymers and CHPs, in a murine intratibial OS tumor model. Furthermore, we used microcomputed tomography analysis to evaluate the bone microarchitecture and correlated bone morphometric parameters (porosity, bone volume, and surface area) with maximum accumulation (S_{max}) and accumulation at 168 h postinjection (S_{168}) of the copolymers at the tumor. Our results provide the foundation for the use of HPMA copolymer–CHP conjugates as targeted drug delivery systems in OS tumors.

Graphical Abstract

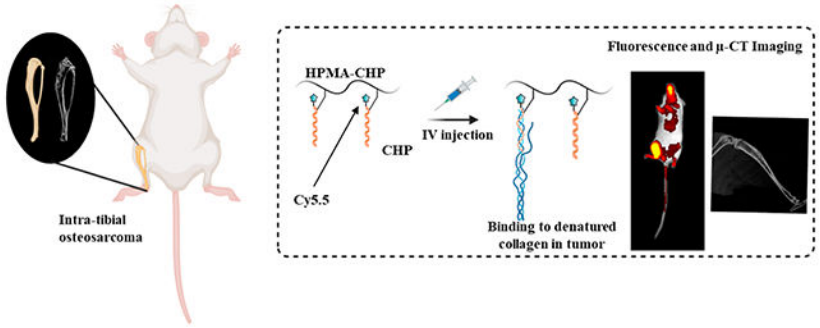

Keywords

collagen; HPMA; osteosarcoma; drug delivery; osteoid extracellular matrix

INTRODUCTION

Osteosarcoma (OS) is the most common form of primary malignant bone cancer in adolescents,[1–3] which typically occurs in the long bones of the appendicular skeleton, most commonly the femur, tibia, or humerus.[3,4] Current therapy includes surgical resection in combination with chemotherapy, but treatment is hampered by systemic side effects and inoperable tumors.[5,6] Neoadjuvant (preoperative) chemotherapy to reduce the tumor size followed by resection has greatly increased the chances of a successful surgery and reduced the need for limb amputation.[7] Adjuvant and neoadjuvant chemotherapy have together brought the 5 year survival rate to 60–70%;[8] however, off-target toxicities severely impact the quality of life.[9] OS treatment would greatly benefit from localized delivery of drugs to the osteoid extracellular matrix tissue to reduce systemic side effects and toxicities. Targeting the extracellular matrix has been increasingly explored for tumor drug delivery.[10]

The bone tissue is composed of a mineralized matrix, in which the organic component is predominantly collagen type I but also includes noncollagenous proteins.[11–13] OS forms in the collagen-rich metaphysis of bone near the growth plate[14] and is accompanied by extensive bone degradation, remodeling, and invasion into surrounding tissues.[15] OS tumors are characterized by upregulated activity of osteoclasts, causing increased bone resorption, followed by compensatory deposition of osteoid ECM by reactive osteoblasts.[16] OS tumors thus involve a complex interplay of lytic (bone resorptive) and blastic (bone building) activity.[17] The high bone remodeling activity of OS is associated with elevated collagenase

activity,[18] which leads to an increased presentation of denatured (monomeric) collagen in OS tumors. Furthermore, the increased bone deposition creates an excess of collagen at the osteoid ECM which is remodeled during mineralization.[19]

Collagen molecules are made up of three individual protein strands folded into a signature triple helix, which is a supercoiled helix of three polyproline II helices.[20] Collagen hybridizing peptides (CHPs) are a class of synthetic peptides with strong triple helical folding propensity similar to naturally occurring collagen and can selectively hybridize to denatured collagen strands by folding into a triple helix. Since conventional CHPs can self-trimerize, losing their ability to target collagen,[21] a new form of CHP-incorporating (4*S*,2*S*)-fluorinated proline ,was developed which has a weaker propensity to self-trimerize at physiological temperature because fluorine causes steric clashes within the homotrimers.[20] In our work, we explored this new form of CHP as a targeting moiety to facilitate delivery to OS tumors.

Water-soluble *N*-(2-hydroxypropyl)methacrylamide (HPMA) copolymers have been extensively studied for tumor targeting and drug delivery.[22–27] They are generally considered to be nontoxic and nonimmunogenic,[23,24] display size-dependent accumulation in solid tumors attributed to the enhanced permeability and retention (EPR) effect,[24,28] and can confer multifunctionality through attachment of drugs, imaging agents, and targeting moieties to synthetically adaptable side chains.[23,29] The use of such water-soluble polymers can improve the pharmacokinetics and delivery of drugs conjugated to the polymer, and attachment of targeting moieties has been shown to improve the binding and localization of polymer conjugates at the target site.[25,26,29]

In this work, we conjugated CHPs to the side chains of HPMA copolymers (HPMA–CHP) and examined HPMA–CHP's localization in tumors in a murine model of intratibial OS (Figure 1). We used polymers with size above the renal threshold to allow for passive accumulation via the EPR effect. Vasculature near the bone has been shown to have fenestrations large enough to accommodate bone extravasation of circulating nanoscale macromolecules such as these.[30,31] We used microcomputed tomography (μ-CT) and bone microarchitecture analysis to extract bone morphometric parameters. We correlated the morphometric parameters in the cortical and trabecular bone with HPMA–CHP accumulation at its maximum tumor accumulation (S_{max}) and its tumor accumulation at 168 h postintravenous administration of experimental compounds in mice bearing established tumors (S_{168}) in order to determine which parameters are potentially associated with accumulation. This study provides the foundation for the use of collagen-targeted HPMA copolymer–CHP conjugates as drug delivery vehicles for OS tumors. The reported μ-CT-based bone morphometric parameters and their correlations with HPMA–CHP accumulation can be further explored in future to inform personalized treatment strategies.

EXPERIMENTAL SECTION

Materials.

(2*S*,4*S*)-Fmoc-4-fluoro-pyrrolidine-2-carboxylic acid was acquired from Chem Impex International (Wood Dale, IL). All other Fmoc-amino acids were acquired

from VWR International (Radnor, PA). *N*,*N*-Dimethylformamide (DMF) and *N*,*N*-diisopropylethylamine (DIPEA) were acquired from Thermo Fisher Scientific (Waltham, MA). Phosphate-buffered saline (PBS) was acquired from ATCC (Manassas, Va). Cyanine5.5 *N*-hydroxysuccinimide (NHS) ester reactive dye was acquired from Lumiprobe (Hunt Valley, MD). All other materials for this study were acquired from Sigma-Aldrich (St. Louis, MO).

Synthesis and Characterization of Copolymer–Peptide Conjugates.

Copolymer conjugates were synthesized according to previously published procedures.[32] Briefly, the comonomers *N*-(2-hydroxypropyl)methacrylamide (HPMA) and *N*-methacryloylglycylglycine (MA-GG-OH) were synthesized according to previously published methods[22] and characterized by electrospray ionization mass spectrometry (ESI-MS) and/or nuclear magnetic resonance (NMR) spectroscopy. Copolymer precursors were synthesized by free-radical copolymerization using azobisisobutyronitrile (AIBN) as an initiator. HPMA (240 mg, 1.70 mmol) and MA-GG-OH (60 mg, 0.30 mmol) were dissolved in 2 mL of DMSO/methanol (2:3) at a molar feed ratio of 85:15 (HPMA/MA-GG-OH) and a total monomer concentration of 1 M. AIBN (12 mg, 0.073 mmol) was added, and the solution was transferred to a 5 mL glass ampule (Thomas Scientific, Swedesboro, NJ). The solution was degassed using freeze–thaw cycles. The ampule was sealed, and the reaction solution was stirred under an inert N_2 atmosphere for 24 h at 50 °C using a temperature-controlled oil bath. The reaction mixture was added to an 80-fold excess volume of acetone to precipitate the product. The precipitates were isolated through centrifugation and decantation, washed twice with acetone, and allowed to dry.

CHP [Cy5.5-KGGG$(GfO)_9$; f: (2*S*, 4*S*)-4-fluoroproline; O: 4-hydroxyproline] and control scrambled peptide ^{S}CHP (Cy5.5-KGGG-OfGGOfGfGfOfOGOfGOOfGGOOffG) (single amino acid abbreviations used) lacking in collagen binding affinity[21] were synthesized by automated Fmoc-mediated solid-phase peptide synthesis (SPPS) using the 2-(1*H*-benzotriazol-1-yl)-1,1,3,3-tetramethyluronium hexafluorophosphate (HBTU) coupling reagent and TentaGel-R-RAM resin and some manual modifications. Cy5.5 NHS ester in 10% DIPEA/DMF solution was added to the resin for attachment to the N-terminus of the peptide. Peptides were cleaved from the resin and deprotected using a standard cleavage cocktail [trifluoroacetic acid (TFA)/water/triisopropyl silane (TIPS) = 95:2.5:2.5 by volume], which produced unreactive amide at the C-terminus. The deprotected lysine side chain provides a primary amine for conjugation to the side chains of the HPMA copolymers. Cleaved peptides were purified using reverse-phase high-performance liquid chromatography (HPLC) [Agilent SD-1 PrepStar HPLC pump and a Zorbax 300SB-C18 column (Agilent)]. The molecular mass of the peptides (MW = 3449 g/mol) was confirmed using a matrix-assisted laser desorption ionization time-of-flight (MALDI-TOF; Bruker UltrafleXtreme) mass spectrometer. Cyanine5.5 (Cy5.5) is a fluorophore for in vivo fluorescence detection, and Gly-Gly-Gly was used as a flexible spacer to decouple the peptide from the polymer backbone.

CHPs were conjugated to the side chains of HPMA copolymer precursors using 1-ethyl-3-(3-dimethylaminopropyl)carbodiimide (EDC) coupling chemistry at 55 °C in a

temperature-controlled oil bath. Peptides (6 mM, 1 mL) and copolymer precursor (1.2 mM, 1 mL) were separately dissolved in 10% DIPEA/DMF and heated to 55 °C. EDC (12 μmol) was added to the copolymer solution, and the mixture was stirred for 5 min. The peptide solution was added, and the reaction was stirred for 24 h at 55 °C. To stop the reaction, the solution was added to an 80-fold excess volume of ether to precipitate the crude product, which was then isolated through centrifugation and decantation. To purify, the product was dialyzed against water at 50 °C for 2 days and lyophilized to produce the final conjugates HPMA–CHP and HPMA–^{S}CHP. A schematic of the HPMA–CHP synthesis is shown in Figure 2. The weight-average molecular weight (M_W), number-average molecular weight (M_N), and dispersity (M_W/M_N) were estimated using size exclusion chromatography (SEC) (Akta fast protein liquid chromatography system, Superose six-column, 10 × 300 mm, PBS eluent) coupled with a differential refractive index detector (OptiLab Rex, Wyatt Technologies Corporation). UV–vis spectrophotometry was used to quantify the peptide content.

Osteosarcoma Model Generation.

Animal experiments were approved by and performed in accordance with University of Utah's Institutional Animal Care and Use Committee (IACUC) guidelines (IACUC #21-10007), with assistance from the Huntsman Cancer Institute's Preclinical Research Resource. Mice were acquired from Charles River Laboratories. To generate an intratibial orthotopic osteosarcoma murine model, NOD scid gamma (NSG) mice were implanted with Saos-2 cells (2.0×10^6 cells/tumor) suspended in 20 μL of PBS in the right proximal tibia. Tumors were grown for 4 weeks to allow for the development of established tumors prior to polymer administration. Mice were given an alfalfa-free diet to reduce interference during fluorescence imaging.

Polymer Administration and Imaging.

The right legs of mice were treated with depilatory cream (Nair) to reduce autofluorescence and maximize the detection of the fluorescent signal. Four weeks post-tumor-cell injection, mice (n = 6 per group) were administered via tail vein injection 10 nmol equivalent of CHP content (as determined by Cy5.5 concentration) as HPMA–CHP, HPMA–^{S}CHP, or CHP in 200 μL of PBS solution. Fluorescence imaging was done in mice at t = 0 (preinjection of polymers or peptides), 0.1 (immediately postinjection), 6, 12, 24, 48, 72, 96, 120, 144, and 168 h using an in vivo imaging system IVIS Spectrum (Caliper LifeSciences, Waltham, MA), using an excitation wavelength of 675 nm and an emission wavelength of 720 nm. Regions of interest (ROIs) surrounding the proximal tibia, which were equivalent for all animals, were selected and used to quantify the total radiant efficiency and accumulation of compounds at the tumor. Mice were also imaged, using planar X-ray imaging, 1 day prior to sacrifice for tumor growth and bone condition using a Faxitron UltraFocus^{DXA} small-animal dual-energy X-ray system (Hologic, Tucson, AZ).

Necropsy and Organ Accumulation.

Mice were euthanized at the 168 h time point using CO_2 inhalation and cervical dislocation. The organs (heart, lungs, liver, spleen, stomach and intestines, and kidneys) and the tumor-bearing right leg were harvested. The right leg was removed from the femoral head to the

foot. The skin was removed, but the remaining soft tissue was left intact. Organs and legs were imaged for fluorescence using an IVIS as described above. ROIs of equivalent area for a given organ or leg were selected, and the total radiant efficiency was measured and quantified for comparison of organ accumulation. The tumor-bearing legs were fixed in 10% neutral buffered formalin for 24 h, rinsed in PBS for 5 min, and stored in 70% ethanol at 4 °C.

μ-CT Imaging.

Ex vivo μ-CT imaging was performed on fixed tumor-bearing legs using a small animal Quantum GX μ-CT scanner (PerkinElmer, Waltham, MA). Bone μ-CT images were acquired using 4 min scans at 90 kV and 88 μA current and reconstructed at a 50 μm voxel size. Reconstructed images were processed using Analyze 14.0 software (AnalyzeDirect, Overland Park, KS).

Bone Microarchitecture Analysis.

To extract bone morphometric parameters related to porosity, surface area, and volume, images were processed using Analyze 14.0 software with a Bone Microarchitecture Analysis add-on (AnalyzeDirect). Images were oriented to align the transaxial plane perpendicular to the length of the tibia. The object was segmented to isolate the tibia. Segmented tibial bone maps were further separated into the cortical bone, trabecular bone, and intratrabecular space. Bone morphometric parameters of the whole tibia were extracted using the software described above. Pearson's correlation coefficient r was used to assess correlations between parameters and maximum accumulation (S_{max}) or accumulation at 168 h (S_{168}) values for HPMA–CHP, HPMA–^{S}CHP, and CHP, and p values were used to assess the significance of the correlations.

Statistical Analysis.

The significance of experiments comparing fluorescent signals and pharmacokinetic parameters was determined using the unpaired t-test between groups, with a significance level of $\alpha = 0.05$. For correlation experiments, Pearson's correlation coefficient r was used to assess the correlation, and p values were used to determine the significance of the observed correlation, with a presentation of weak correlations at a significance of $\alpha = 0.1$.

RESULTS

Synthesis and Characterization of HPMA–CHP, HPMA–^{S}CHP, and CHP.

HPMA copolymer precursors were synthesized by free-radical copolymerization of comonomers HPMA and MA-GG-OH using the initiator AIBN. M_W, M_N, and dispersity (M_W/M_N) were 85, 47 kDa, and 1.8, respectively. CHP and scrambled peptide (^{S}CHP) were synthesized by SPPS with on-resin manual addition of Cy5.5. Peptides were conjugated to copolymer precursors using EDC coupling chemistry. Purified conjugates, HPMA–CHP and HPMA–^{S}CHP, contained on average 1.8 and 3.7 peptides per polymer chain, respectively. Selective binding of HPMA–CHP to denatured collagen was verified previously.[32] Although the conjugation efficiency was lower for targeted peptides than scrambled peptides, collagen

binding experiments demonstrated significantly more collagen binding for HPMA–CHP conjugates than for HPMA–^{S}CHP conjugates.[32]

HPMA–CHP Had Higher Accumulation and Retention Compared to HPMA–^{S}CHP in Murine Tumor-Bearing Tibia.

NSG mice bearing osteosarcoma tumors, induced by injecting Saos-2 cells into the right proximal tibia, were administered with Cy5.5-labeled HPMA–CHP, HPMA–^{S}CHP, or CHP (N = 6 mice per group) via tail vein injection. Fluorescent signals (ex: 675 nm; em: 720 nm) were measured at t = 0 (preinjection), 0.1 (postinjection), 6, 12, 24, 48, 72, 96, 120, 144, and 168 h postinjection (Figure 3). One mouse from each group was randomly selected at the start of the study and used in all representative images. The remaining five mice in each group were imaged groupwise. All images are presented in the Supporting Information (Figures S1–S4). The fluorescent signal (in radiant efficiency) at the tibia was quantified over time (Figure 4a). Semiquantitative noncompartmental pharmacokinetic analysis showed the area under the curve (AUC, radiant efficiency × h) of HPMA–CHP to be 1.8×10^{12}, which was 1.6 times higher than that of HPMA–^{S}CHP, which was 1.1×10^{12} (Figure 4b and Table 1). The tumor half-lives ($t_{1/2}$) of HPMA–CHP and HPMA–^{S}CHP were 97.9 and 77.8 h, respectively. The maximum accumulation (S_{max}) values of HPMA–CHP and HPMA–^{S}CHP corresponded to 1.9×10^{10} and 1.1×10^{10} radiant efficiency units, respectively, with time to maximum accumulation (t_{max}) values of ~6 and ~24 h, respectively. HPMA–CHP compared to HPMA–^{S}CHP showed higher accumulation at most time points (Figure 4c).

HPMA–CHP Showed Greater Retention in Osteosarcoma Tumors than CHP.

Compared to CHP, HPMA–CHP had similar accumulation at the tumor through the 120 h time point but higher accumulation at t = 144 and 168 h (Figure 4c). HPMA–CHP also showed a significantly longer half-life than CHP, with 97.9 h for HPMA–CHP and 67.5 h for CHP (Figure 4b and Table 1). HPMA–CHP and CHP had S_{max} values of 1.9×10^{10} rad eff and 2.3×10^{10} rad eff, respectively. Both had t_{max} values of ~6 h. The difference in AUC was not significant: 1.8×10^{12} rad eff × h for HPMA–CHP compared to 1.5×10^{12} rad eff × h for CHP.

Organs Harvested at 168 h Show Differences in Accumulation between HPMA–CHP, HPMA–^{S}CHP, and CHP.

To better measure organ accumulation, mice were euthanized at 168 h, and the heart (h), lungs (lg), liver (lv), spleen (s), stomach and intestines (s&i), kidneys (k), and the tumor-bearing right leg (leg) were harvested, and the fluorescent signal was measured (Figure 5a). Fluorescence images of organs of all mice are shown in the Supporting Information (Figures S5–S7). HPMA–CHP showed higher accumulation in all organs and the tumor compared to HPMA–^{S}CHP (Figure 5b). HPMA–CHP showed higher accumulation in the liver and spleen and lower accumulation in the kidneys, compared to CHP, with no significant differences in other organs and the tumor-bearing leg.

μ-CT and Bone Microarchitecture Analysis Show Cortical Porosity Is Directly Correlated with Polymer Accumulation.

Ex vivo tibias of mice were scanned by μ-CT, and resulting 3D reconstructions were segmented and analyzed using the Bone Microarchitecture Analysis tool of AnalyzeDirect 14.0 software. Bone morphometric parameters, listed in Table S1, were extracted for the total bone, cortex, intratrabecular region, trabecular bone, total trabecular tissue, and whole tissue. Pearson's correlation coefficient r values were calculated for each compound's S_{168} and S_{max}, in radiant efficiency, with respect to each parameter using the GraphPad Prism (Table S1). One tibia replicate in the HPMA–^{S}CHP experimental group was degraded too extensively for software to resolve tissue boundaries and extract parameters. Values associated with this replicate have been excluded, and the HPMA–^{S}CHP has $n = 5$.

Values associated with cortical porosity, bone volume, and bone surface area with Pearson's r greater than 0.7 were graphed against S_{168} values (Figure 6), along with p values and 95% confidence intervals. $\alpha = 0.1$ was used to assess significance. Cortical porosity parameters showed a correlation with HPMA–CHP and HPMA–^{S}CHP accumulation. Other parameters showed high correlations but were not significant, likely due to a small sample size.

DISCUSSION

The organic component of bone is composed of more than 90% of type I collagen.[13,33,34] During physiological bone remodeling, beginning with bone resorption, an acidic environment is induced by osteoclast activity which dissolves hydroxyapatite, the inorganic component of bone, and exposes type I collagen.[13,34,35] The acidity also promotes the activity of cysteine proteases, such as cathepsin K, which degrade the collagen.[35] Following this, during bone formation, osteoblasts produce and deposit more osteoid ECM including collagen which is further remodeled for mineralization.[35] Additionally, another type of cells, reversal cells, support the removal of collagen fragments from the degraded bone surface, also through collagenolytic activity. These processes are enhanced and dysregulated during OS tumor progression, which is accompanied by extensive bone remodeling and leads to an increased presentation of the degraded bone surface and monomeric collagen.[15,36] Additionally, Saos-2 OS tumors are associated with increased expression of type I collagen.[37] The bone degradation processes that occur in osteosarcoma are similar to those that occur in bone metastasis. Overall, although OS tumors are generally lytic, they exhibit osteoblast activity and increased deposition of the osteoid matrix.

In this study, we found that our denatured collagen-targeting polymer (HPMA–CHP) showed a higher sustained residence at the tumor compared to both the nontargeted polymer (HPMA–^{S}CHP) and the peptide (CHP) itself (Figure 4). Furthermore, the targeted polymer had a similar t_{max} as the peptide (~6 h), while the nontargeted polymer had a t_{max} (~24 h) at a later time point (Table 1). The vasculature surrounding a bone is known to have fenestrations up to 80 nm[30] (larger than the hydrodynamic diameter of the polymer constructs used here). While changes in vasculature and fenestrations due to tumor growth likely played a substantial role in extravasation, the earlier t_{max} for HPMA–CHP (similar to CHP) compared to HPMA–^{S}CHP suggests that binding to degraded collagen in the bone appears to have played a major role in retention. Previously, we administered these

three compounds in breast tumor-bearing mice and found that both polymers, targeted and nontargeted, had similar t_{max} values of ~24 h while the peptide had a t_{max} of ~6 h,[32] which may reflect a difference between the vasculature and extravasation at the bone versus the breast tumor tissue. In the OS tumors, the targeted polymer had a higher AUC than the nontargeted polymer (Figure 4B), indicating that targeting remodeling collagen may elicit a higher potential drug exposure if used as a drug delivery vehicle. Between the targeted polymer and the peptide, the accumulations at the tumor until the 144 h time point were similar (Figure 4C). From 144 h onward, the accumulation of the targeted polymer was higher, indicating that the CHP was cleared faster than HPMA–CHP. Between the targeted polymer and the nontargeted polymer, the targeted polymer had higher accumulation at initial and later time points, while the accumulations at middle time points were not statistically different. The targeted polymer consistently had higher accumulation than the nontargeted polymer, and likely the fluctuation of statistical significance could be due to the small sample size.

For organ distribution analysis, the targeted polymer had a higher accumulation in all organs and the tumor-bearing leg compared to the nontargeted polymer (Figure 5). Collagen is remodeled as a part of normal tissue maintenance, and the higher level of binding of the targeted polymer may be due to a basal level of denatured collagen. The relative distribution of signal (which is semiquantitative given the differences in tissue penetration of signal) between organs is comparable to what has been seen in our previous work in a breast cancer model.[32] While the signal at the heart is very low in all three, the higher level seen in the heart for HPMA–CHP compared to HPMA–^{S}CHP may be due to a higher amount in circulation at the 168 h time point, which may have only been washed away from the tumor and other organs at a later time point and thus remains in the bloodstream at this time. The higher levels of accumulation in the kidneys and liver compared to organs could be related to excretion. Additionally, the differences between targeted and nontargeted polymers in these organs may be related to the timing of excretion, that is, the targeted polymer was still present due to prolonged binding at the tumor, while the nontargeted polymer was excreted prior to this 168 h time point. Increasing the CHP content may serve as a strategy to promote retention at the tumor and further improve localization in the tumor compared to healthy organs. Between HPMA–CHP and CHP, the accumulation in the leg, heart, lungs, and stomach and intestines were similar. This supports that collagen binding plays a role in off-target binding to remodeling collagen. HPMA–CHP had a higher accumulation in the liver and spleen, while CHP had a higher accumulation in the kidneys. The differences in liver and kidney values are likely related to the excretion mechanisms of the two constructs, while that in spleen might be related to the high vascularity of the spleen, allowing increased accumulation with increased circulation, coupled with increased retention of HPMA–CHP.

Osteosarcoma tumors are heterogeneous[14] and both intra-tumoral and intertumoral heterogeneities make targeting difficult.[14] Osteosarcoma causes changes in the structural integrity of bone,[16] which might contribute to the degree of polymer or peptide extravasation or retention at the bone as well as the amount of denatured collagen. Bone is composed of a hard outer bone called the cortex and an inner porous spongy bone called the trabeculae.[16] Several bone remodeling changes, and consequently, measurable bone properties, are known to be associated with osteosarcoma. These include weakening of cortical integrity associated

with enzyme digestion and tumor penetration into the soft tissue surrounding the bone and changes in the trabecular bone tissue.[37,38] Correlating the specific bone parameters, which can be obtained using CT imaging, a common and noninvasive medical imaging technique, with the likelihood of targeting and polymer accumulation could inform a personalized treatment strategy and predict the utility of a polymer-based system. In this study, with limited power to conclude the significance of correlations due to the small sample size, we found that several parameters showed a correlation with accumulation. Cortical porosity, the fraction of void volume within the cortical bone,[39] is highly linked with bone remodeling[40] and displayed a correlation with the accumulation of targeted polymer at 168 h (S_{168}) (Figure 6). The p values indicate that it is weakly significant (using $\alpha = 0.1$). Cortical porosity appears to be correlated (albeit weakly, due to a small sample size) with polymer accumulation (targeted and nontargeted) but not with peptide accumulation (Table S1). This would suggest that a larger study varying the cortical porosity and measuring the polymer accumulation could help elucidate a relationship that might inform treatment strategies.

There are several bone-targeted delivery systems that have been explored.[41–44] Some well-known examples of moieties employed to target nanoplatforms to bone include bisphosphonates, tetracyclines, and bone sialoproteins,[45,46] which, like in most strategies currently used, bind to hydroxyapatite minerals in the bone matrix.[30] Several of these moieties have been associated with toxicities, including pediatric growth inhibition and osteonecrosis of the jaw.[47–49] Polymers have been employed to target the bone predominantly through binding to hydroxyapatite.[41,42,46,50,51] HPMA copolymers have been targeted to the bone using the hydroxyapatite-binding moieties Asp8 and alendronate. HPMA copolymer–Asp8 conjugates showed improved polymer accumulation compared to HPMA alone.[52] Furthermore, the study showed that higher-molecular-weight HPMA copolymers demonstrated higher accumulation than lower-molecular-weight polymers due to extended circulation time and discontinuous blood vessels in the bone marrow.[52] Another study showed that the medium-molecular-weight HPMA–alendronate polymer conjugates (50–100 kDa) showed the most binding compared to larger or smaller polymers.[53] PEG has also been explored as a polymer carrier to target the bone.[46] Additionally, it has been shown that there is higher accumulation in regions of high bone turnover in the metaphyseal region,[54] which is the common site of osteosarcoma. The targeted system in this study binds to collagen, which makes up a high proportion of bone tissues including nonmineralized bones such as the cartilage.[33,35] Since bone destruction involves extensive collagen degradation and demineralization, targeting collagen instead of bone minerals could be an advantage. Its lack of toxicity and adaptability also provide an advantage as a versatile platform.

CONCLUSIONS

This study extends the applicability of collagen-targeted water-soluble copolymer conjugates in primary bone cancer. The copolymer–peptide conjugate showed an increased accumulation and retention at the tumor compared to the nontargeted conjugate as well as an increase in retention over the peptide alone. In future studies, expanding the μ-CT analysis to measure relationships between bone parameters, polymer accumulation in the bone tumor at different time points, and tumor stages could help elucidate mechanisms that promote

targeting and retention at the bone. Furthermore, this conjugate can be employed as a drug delivery vehicle or diagnostic tool for the management of OS.

Supplementary Material

Refer to Web version on PubMed Central for supplementary material.

ACKNOWLEDGMENTS

The authors would like to thank Dr. Jaime Fornetti for numerous discussions and advice. This work was funded by the Ruth L. Kirschstein National Institutes of Health (NIH)'s National Research Service Award (NRSA) awarded to N.S. (5F31CA213901) and NIH R21OD026618 awarded to S.M.Y. The authors would also like to acknowledge the Preclinical Research Resource (PRR) at the Huntsman Cancer Institute (HCI), supported by the National Cancer Institute (NCI) of the NIH under Award Number P30CA042014, for their assistance with in vivo experiments. Figures were made with the help of BioRender.com.

ABBREVIATIONS

μ-CT	microcomputed tomography
AIBN	azobisisobutyronitrile
AUC	area under the curve
CHP	collagen hybridizing peptide
^{S}CHP	scrambled CHP
CI	confidence interval
CT	computed tomography
Cy5.5	Cyanine5.5
DIPEA	*N*,*N*-diisopropylethylamine
DMF	dimethylformamide
ECM	extracellular matrix
EDC	1-ethyl-3-(3-dimethylaminopropyl)-carbodiimide
ESI-MS	electrospray ionization mass spectrometry
HBTU	2-(1*H*-benzotriazol-1-yl)-1,1,3,3-tetramethyluronium hexafluorophosphate
HPLC	high-performance liquid chromatography
HPMA	*N*-(2-hydroxypropyl)-methacrylamide
HPMA–CHP	HPMA copolymer–CHP conjugate
HPMA–^{S}CHP	HPMA copolymer-scrambled CHP conjugate
IACUC	Institutional Animal Care and Use Committee

IV	intravenous
IVIS	in vivo imaging system
M_N	number-average molecular weight
M_W	weight-average molecular weight
MA-GG-OH	*N*-methacryloylglycylglycine
MALDI-ToF	matrix-assisted laser desorption ionization time-of-flight
NHS	*N*-hydroxysuccinimide
NMR	nuclear magnetic resonance
NOD	nonobese diabetic
NSG	NOD scid gamma
OS	osteosarcoma
PBS	phosphate-buffered saline
ROI	region of interest
S_{168}	accumulation at 168 h
S_{max}	maximum accumulation
SD	standard deviation
SPPS	solid-phase peptide synthesis
$t_{1/2}$	tumor half-life
t_{max}	time to maximum accumulation
UV–vis	ultraviolet–visible

REFERENCES

(1). Yuan J; Ossendorf C; Szatkowski JP; Bronk JT; Maran A; Yaszemski M; Bolander ME; Sarkar G; Fuchs B Osteoblastic and osteolytic human osteosarcomas can be studied with a new xenograft mouse model producing spontaneous metastases. Cancer Invest. 2009, 27, 435–442. [PubMed: 19212826]

(2). Wu K; Yu B; Li D; Tian Y; Liu Y; Jiang J Recent Advances in Nanoplatforms for the Treatment of Osteosarcoma. Front. Oncol 2022, 12, 805978. [PubMed: 35242707]

(3). Ritter J; Bielack SS Osteosarcoma. Ann. Oncol 2010, 21, vii320–vii325. [PubMed: 20943636]

(4). Bacci G; Lari S Current Treatment of High Grade Osteosarcoma of the Extremity: Review. J. Chemother 2001, 13, 235–243. [PubMed: 11450880]

(5). Grünewald TG; Alonso M; Avnet S; Banito A; Burdach S; Cidre-Aranaz F; Di Pompo G; Distel M; Dorado-Garcia H; Garcia-Castro J; González-González L; Grigoriadis AE; Kasan M; Koelsche C; Krumbholz M; Lecanda F; Lemma S; Longo DL; Madrigal-Esquivel C; Morales-Molina Á.; Musa J; Ohmura S; Ory B; Pereira-Silva M; Perut F; Rodriguez R; Seeling C; Al Shaaili N; Shaabani S; Shiavone K; Sinha S; Tomazou EM; Trautmann M; Vela M; Versleijen-

Jonkers YM; Visgauss J; Zalacain M; Schober SJ; Lissat A; English WR; Baldini N; Heymann D Sarcoma treatment in the era of molecular medicine. EMBO Mol. Med 2020, 12, No. e11131. [PubMed: 33047515]

(6). Fernandes I; Melo-Alvim C; Lopes-Brás R; Esperança-Martins M; Costa L Osteosarcoma Pathogenesis Leads the Way to New Target Treatments. Int. J. Mol. Sci 2021, 22, 813. [PubMed: 33467481]

(7). Yuan G; Chen J; Wu D; Gao C Neoadjuvant chemotherapy combined with limb salvage surgery in patients with limb osteosarcoma of Enneking stage II: a retrospective study. OncoTargets Ther. 2017, 10, 2745–2750.

(8). Liao J; Han R; Wu Y; Qian Z Review of a new bone tumor therapy strategy based on bifunctional biomaterials. Bone Res. 2021, 9, 18. [PubMed: 33727543]

(9). Zhang Y; Yang J; Zhao N; Wang C; Kamar S; Zhou Y; He Z; Yang J; Sun B; Shi X; Han L; Yang Z Progress in the chemotherapeutic treatment of osteosarcoma. Oncol. Lett 2018, 16, 6228–6237. [PubMed: 30405759]

(10). Subrahmanyam N; Ghandehari H Harnessing Extracellular Matrix Biology for Tumor Drug Delivery. J. Pers. Med 2021, 11, 88. [PubMed: 33572559]

(11). Kolb AD; Bussard KM The Bone Extracellular Matrix as an Ideal Milieu for Cancer Cell Metastases. Cancers 2019, 11, 1020. [PubMed: 31330786]

(12). Rotman SG; Grijpma DW; Richards RG; Moriarty TF; Eglin D; Guillaume O Drug delivery systems functionalized with bone mineral seeking agents for bone targeted therapeutics. J. Controlled Release 2018, 269, 88–99.

(13). Boskey AL Bone composition: relationship to bone fragility and antiosteoporotic drug effects. BoneKEy Rep. 2013, 2, 447. [PubMed: 24501681]

(14). Corre I; Verrecchia F; Crenn V; Redini F; Trichet V The Osteosarcoma Microenvironment: A Complex But Targetable Ecosystem. Cells 2020, 9, 976. [PubMed: 32326444]

(15). Ingvarsen SZ; Gårdsvoll H; van Putten S; Nørregaard KS; Krigslund O; Meilstrup JA; Tran C; Jürgensen HJ; Melander MC; Nielsen CH; Kjaer A; Bugge TH; Engelholm LH; Behrendt N Tumor cell MT1-MMP is dispensable for osteosarcoma tumor growth, bone degradation and lung metastasis. Sci. Rep 2020, 10, 19138. [PubMed: 33154487]

(16). Shoaib Z; Fan TM; Irudayaraj JMK Osteosarcoma mechanobiology and therapeutic targets. Br. J. Pharmacol 2022, 179, 201–217. [PubMed: 34679192]

(17). De Martino V; Rossi M; Battafarano G; Pepe J; Minisola S; Del Fattore A Extracellular Vesicles in Osteosarcoma: Antagonists or Therapeutic Agents? Int. J. Mol. Sci 2021, 22, 12586. [PubMed: 34830463]

(18). Holliday LS; Welgus HG; Fliszar CJ; Veith GM; Jeffrey JJ; Gluck SL Initiation of Osteoclast Bone Resorption by Interstitial Collagenase. J. Biol. Chem 1997, 272, 22053–22058. [PubMed: 9268345]

(19). Misaghi A; Goldin A; Awad M; Kulidjian AA Osteosarcoma: a comprehensive review. SICOT J. 2018, 4, 12. [PubMed: 29629690]

(20). Bennink LL; Li Y; Kim B; Shin IJ; San BH; Zangari M; Yoon D; Yu SM Visualizing collagen proteolysis by peptide hybridization: From 3D cell culture to in vivo imaging. Biomaterials 2018, 183, 67–76. [PubMed: 30149231]

(21). Li Y; Foss CA; Summerfield DD; Doyle JJ; Torok CM; Dietz HC; Pomper MG; Yu SM Targeting collagen strands by photo-triggered triple-helix hybridization. Proc. Natl. Acad. Sci. U.S.A 2012, 109, 14767–14772. [PubMed: 22927373]

(22). Strohalm J; Kopeček J Poly[N-(2-hydroxypropyl)-methacrylamide]. IV. Heterogeneous polymerization. Angew. Makromol. Chem 1978, 70, 109–118.

(23). Yang J; Kopeček J Design of smart HPMA copolymer-based nanomedicines. J. Controlled Release 2016, 240, 9–23.

(24). Yang J; Kopeček J The Light at the End of the Tunnel-Second Generation HPMA Conjugates for Cancer Treatment. Curr. Opin. Colloid Interface Sci 2017, 31, 30–42. [PubMed: 29276426]

(25). Frazier N; Payne A; de Bever J; Dillon C; Panda A; Subrahmanyam N; Ghandehari H High intensity focused ultrasound hyperthermia for enhanced macromolecular delivery. J. Controlled Release 2016, 241, 186–193.

(26). Buckway B; Wang Y; Ray A; Ghandehari H Overcoming the stromal barrier for targeted delivery of HPMA copolymers to pancreatic tumors. Int. J. Pharm 2013, 456, 202–211. [PubMed: 23933441]

(27). Frazier N; Payne A; Dillon C; Subrahmanyam N; Ghandehari H Enhanced efficacy of combination heat shock targeted polymer therapeutics with high intensity focused ultrasound. Nanomedicine 2017, 13, 1235–1243. [PubMed: 27913213]

(28). Matsumura Y; Maeda H A new concept for macromolecular therapeutics in cancer chemotherapy: mechanism of tumoritropic accumulation of proteins and the antitumor agent smancs. Cancer Res. 1986, 46, 6387. [PubMed: 2946403]

(29). Pike DB; Ghandehari H HPMA copolymer–cyclic RGD conjugates for tumor targeting. Adv. Drug Delivery Rev 2010, 62, 167–183.

(30). Low SA; Kopeček J Targeting polymer therapeutics to bone. Adv. Drug Delivery Rev 2012, 64, 1189–1204.

(31). Howlett CR; Dickson M; Sheridan AK The fine structure of the proximal growth plate of the avian tibia: vascular supply. J. Anat 1984, 139, 115. [PubMed: 6469851]

(32). Subrahmanyam N; Yathavan B; Kessler J; Yu SM; Ghandehari H HPMA copolymer-collagen hybridizing peptide conjugates targeted to breast tumor extracellular matrix. J. Controlled Release 2022, 353, 278.

(33). Lynch CC Matrix metalloproteinases as master regulators of the vicious cycle of bone metastasis. Bone 2011, 48, 44–53. [PubMed: 20601294]

(34). Feng X. Chemical and Biochemical Basis of Cell-Bone Matrix Interaction in Health and Disease. Curr. Chem. Biol 2009, 3, 189–196. [PubMed: 20161446]

(35). Nørregaard KS; Jürgensen HJ; Gårdsvoll H; Engelholm LH; Behrendt N; Søe K Osteosarcoma and Metastasis Associated Bone Degradation-A Tale of Osteoclast and Malignant Cell Cooperativity. Int. J. Mol. Sci 2021, 22, 6865. [PubMed: 34202300]

(36). Cui J; Dean D; Hornicek FJ; Chen Z; Duan Z The role of extracelluar matrix in osteosarcoma progression and metastasis. J. Exp. Clin. Cancer Res 2020, 39, 178. [PubMed: 32887645]

(37). Broadhead ML; Clark JCM; Myers DE; Dass CR; Choong PFM The Molecular Pathogenesis of Osteosarcoma: A Review. Sarcoma 2011, 2011, 959248. [PubMed: 21559216]

(38). Jung J-H; Huh K-H; Yong T-H; Kang J-H; Kim J-E; Yi W-J; Heo M-S; Lee S-S Differentiation of osteosarcoma from osteomyelitis using microarchitectural analysis on panoramic radiographs. Sci. Rep 2022, 12, 12339. [PubMed: 35853929]

(39). Bjørnerem Å. The clinical contribution of cortical porosity to fragility fractures. BoneKEy Rep. 2016, 5, 846. [PubMed: 27818743]

(40). Harrison KD; Hiebert BD; Panahifar A; Andronowski JM; Ashique AM; King GA; Arnason T; Swekla KJ; Pivonka P; Cooper DM Cortical Bone Porosity in Rabbit Models of Osteoporosis. J. Bone Miner. Res 2020, 35, 2211–2228. [PubMed: 32614975]

(41). Segal E; Pan H; Benayoun L, Kopečková P; Shaked Y; Kopeček J; Satchi-Fainaro R Enhanced anti-tumor activity and safety profile of targeted nano-scaled HPMA copolymer-alendronate-TNP-470 conjugate in the treatment of bone malignances. Biomaterials 2011, 32, 4450–4463. [PubMed: 21429572]

(42). Segal E; Pan H; Ofek P; Udagawa T; Kopečková P; Kopeček J; Satchi-Fainaro R Targeting angiogenesis-dependent calcified neoplasms using combined polymer therapeutics. PLoS One 2009, 4, No. e5233. [PubMed: 19381291]

(43). Zhou X; Cornel EJ; He S; Du J Recent advances in bone-targeting nanoparticles for biomedical applications. Mater. Chem. Front 2021, 5, 6735–6759.

(44). Katsumi H; Yamashita S; Morishita M; Yamamoto A Bone-Targeted Drug Delivery Systems and Strategies for Treatment of Bone Metastasis. Chem. Pharm. Bull 2020, 68, 560–566.

(45). Zhou X; Cornel EJ; Fan Z; He S; Du J Bone-Targeting Polymer Vesicles for Effective Therapy of Osteoporosis. Nano Lett. 2021, 21, 7998–8007. [PubMed: 34529430]

(46). Wang D; Miller SC; Kopeckova P; Kopecek J Bone-targeting macromolecular therapeutics. Adv. Drug Delivery Rev 2005, 57, 1049–1076.

(47). Chen Y; Wu X; Li J; Jiang Y; Xu K; Su J Bone-Targeted Nanoparticle Drug Delivery System: An Emerging Strategy for Bone-Related Disease. Front. Pharmacol 2022, 13, 909408. [PubMed: 35712701]

(48). Wutzl A; Eisenmenger G; Hoffmann M; Czerny C; Moser D; Pietschmann P; Ewers R; Baumann A Osteonecrosis of the jaws and bisphosphonate treatment in cancer patients. Wien. Klin. Wochenschr 2006, 118, 473–478. [PubMed: 16957978]

(49). Labrinidis A; Hay S; Liapis V; Findlay DM; Evdokiou A Zoledronic acid protects against osteosarcoma-induced bone destruction but lacks efficacy against pulmonary metastases in a syngeneic rat model. Int. J. Cancer 2010, 127, 345. [PubMed: 19924813]

(50). Miller K; Eldar-Boock A; Polyak D; Segal E; Benayoun L; Shaked Y; Satchi-Fainaro R Antiangiogenic antitumor activity of HPMA copolymer-paclitaxel-alendronate conjugate on breast cancer bone metastasis mouse model. Mol. Pharm 2011, 8, 1052–1062. [PubMed: 21545170]

(51). Miller K; Clementi C; Polyak D; Eldar-Boock A; Benayoun L; Barshack I; Shaked Y; Pasut G; Satchi-Fainaro R Poly(ethylene glycol)-paclitaxel-alendronate self-assembled micelles for the targeted treatment of breast cancer bone metastases. Biomaterials 2013, 34, 3795–3806. [PubMed: 23434349]

(52). Pan H; Sima M; Miller SC; Kopečková P; Yang J; Kopeček J Efficiency of high molecular weight backbone degradable HPMA copolymer-prostaglandin E1 conjugate in promotion of bone formation in ovariectomized rats. Biomaterials 2013, 34, 6528–6538. [PubMed: 23731780]

(53). Pan H; Sima M; Kopečková P; Wu K; Gao S; Liu J; Wang D; Miller SC; Kopeček J Biodistribution and pharmacokinetic studies of bone-targeting N-(2-hydroxypropyl)-methacrylamide copolymer-alendronate conjugates. Mol. Pharm 2008, 5, 548–558. [PubMed: 18505266]

(54). Wang D; Sima M; Mosley RL; Davda JP; Tietze N; Miller SC; Gwilt PR; Kopečková P; Kopeček J Pharmacokinetic and biodistribution studies of a bone-targeting drug delivery system based on N-(2-hydroxypropyl)methacrylamide copolymers. Mol. Pharm 2006, 3, 717–725. [PubMed: 17140259]

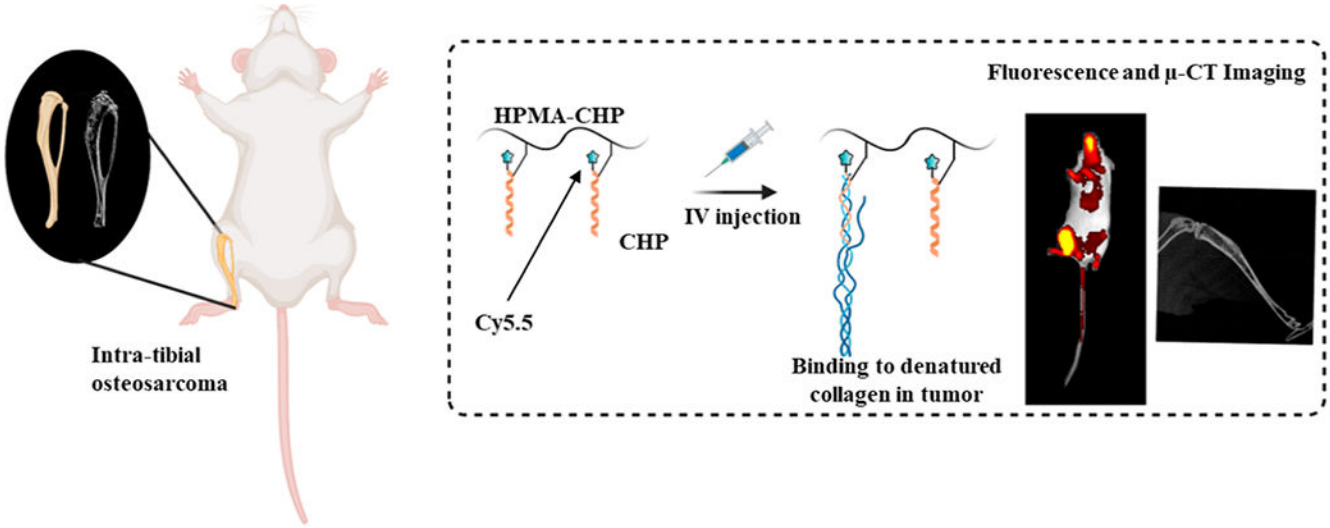

Figure 1.

Schematic of experimental design for HPMA copolymer–CHP conjugates targeting denatured collagen in a murine model of intratibial osteosarcoma.

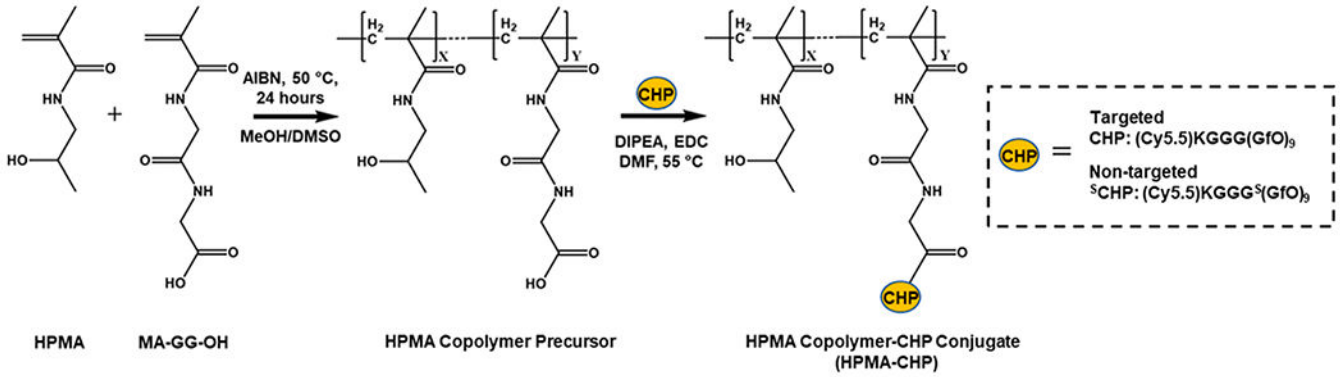

Figure 2.

Schematic of synthesis of HPMA–CHP and HPMA–^{S}CHP conjugates, where $^{S}(GfO)_9$ refers to the scrambled $(GfO)_9$ sequence.

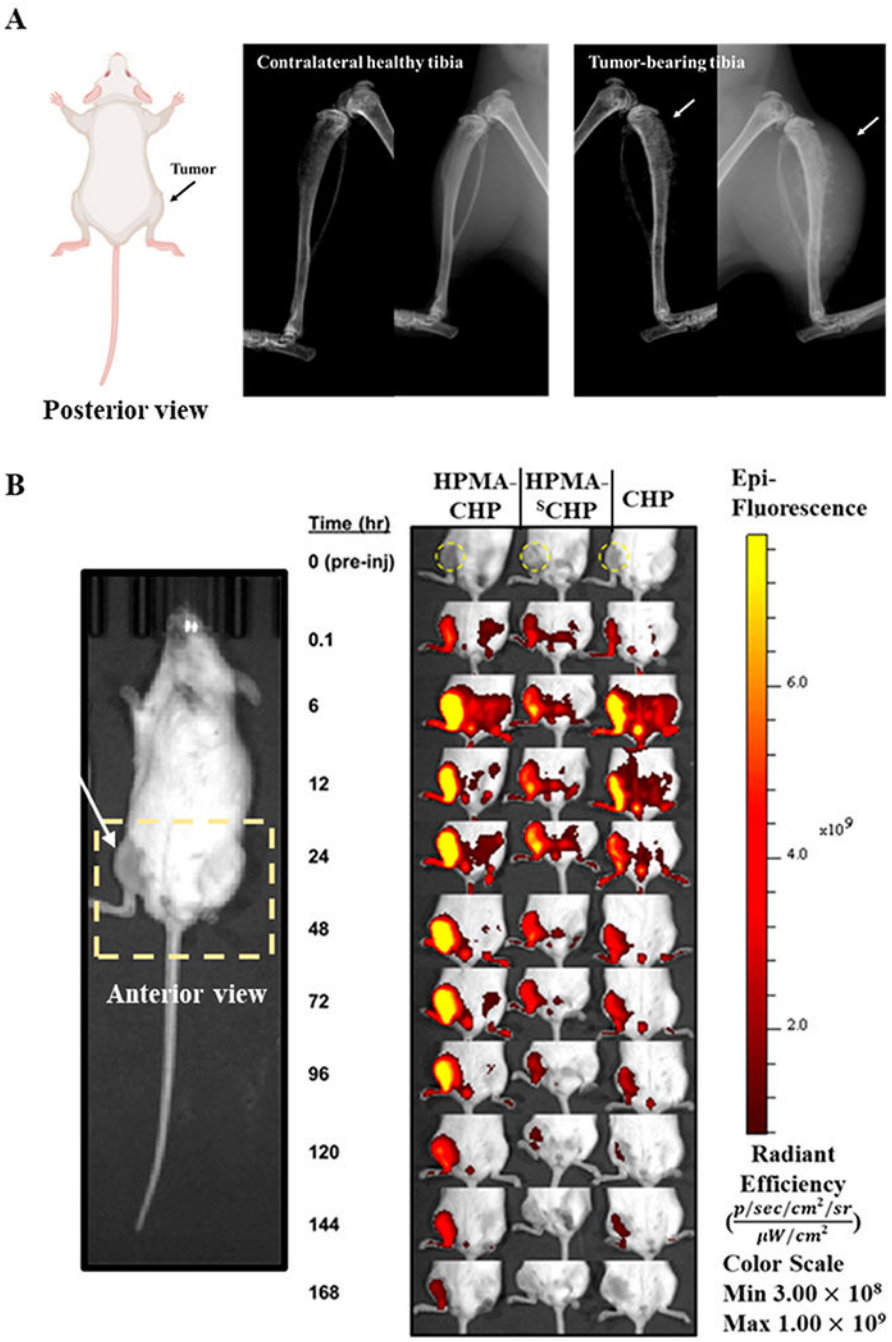

Figure 3.

(A) X-ray images of contralateral and tumor-bearing tibias of osteosarcoma tumor-bearing NSG mice, implanted with Saos-2 cells in the right proximal tibia, each showing the bone alone in the left image and the soft tissue along with the bone in the right image; arrows indicate the tumor site; (B) fluorescence images at $t = 0$ (preinjection), 0.1 (immediately postinjection), 6, 12, 24, 48, 72, 96, 120, 144, and 168 h of intravenously administered HPMA–CHP, HPMA–^{S}CHP, and CHP, with tumor region indicated by the yellow dashed

circle in $t = 0$ preinjection time point image and the rectangular dashed box indicates the cropped region shown in the time point data with the arrow indicating tumor.

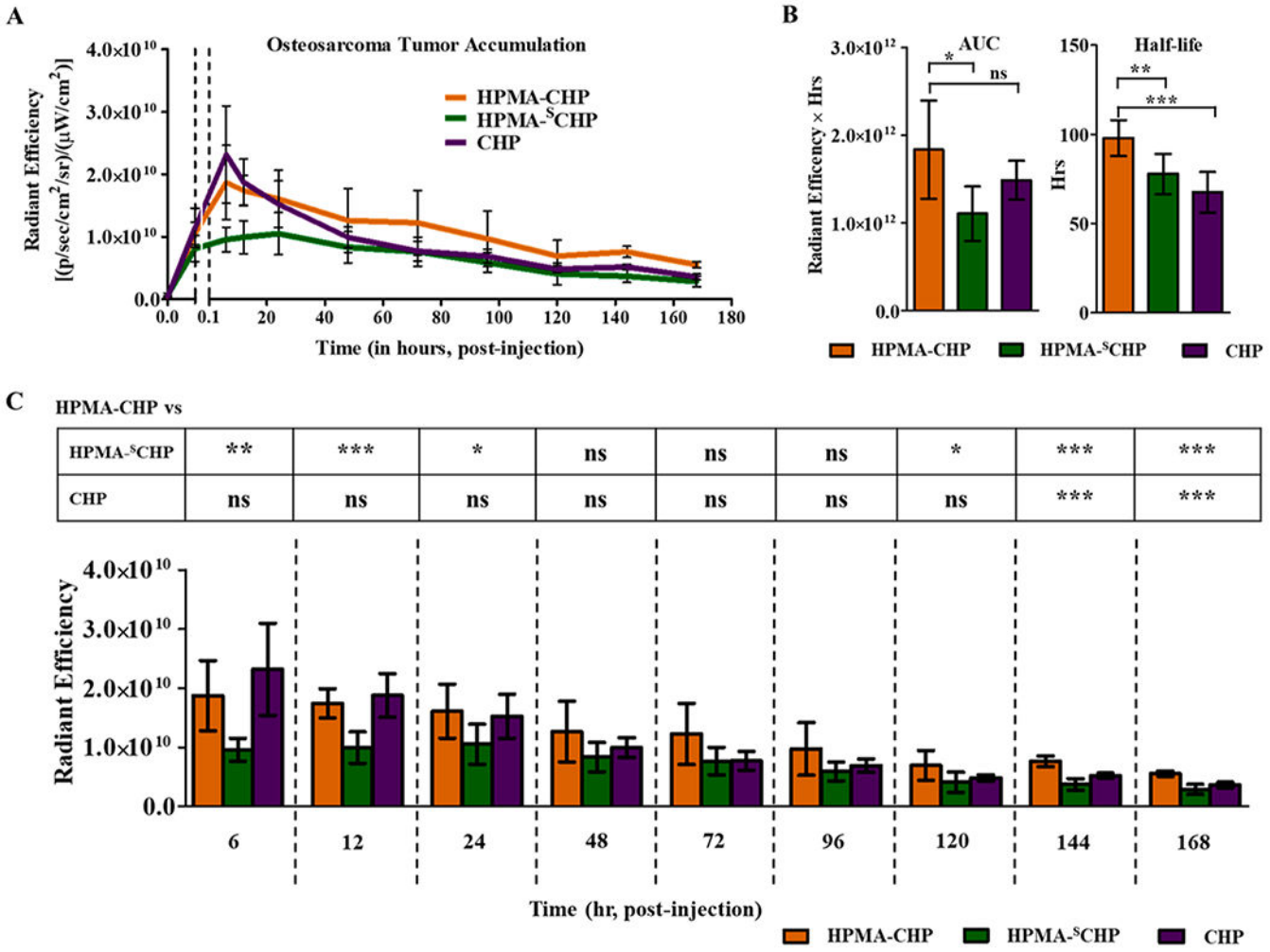

Figure 4.

(A) Postinjection time point radiant efficiencies of tumor region of osteosarcoma tumor-bearing NSG mice after tail vein injection of Cy5.5-labeled HPMA–CHP, HPMA–^{S}CHP, or CHP; (B) AUC and $t_{1/2}$ of compounds at the tumor, calculated using noncompartmental pharmacokinetic analysis; and (C) radiant efficiencies at postinjection time points with corresponding comparative p values (mean ± SD, $N = 6$, *$p < 0.05$, **$p < 0.01$, and ***$p < 0.001$).

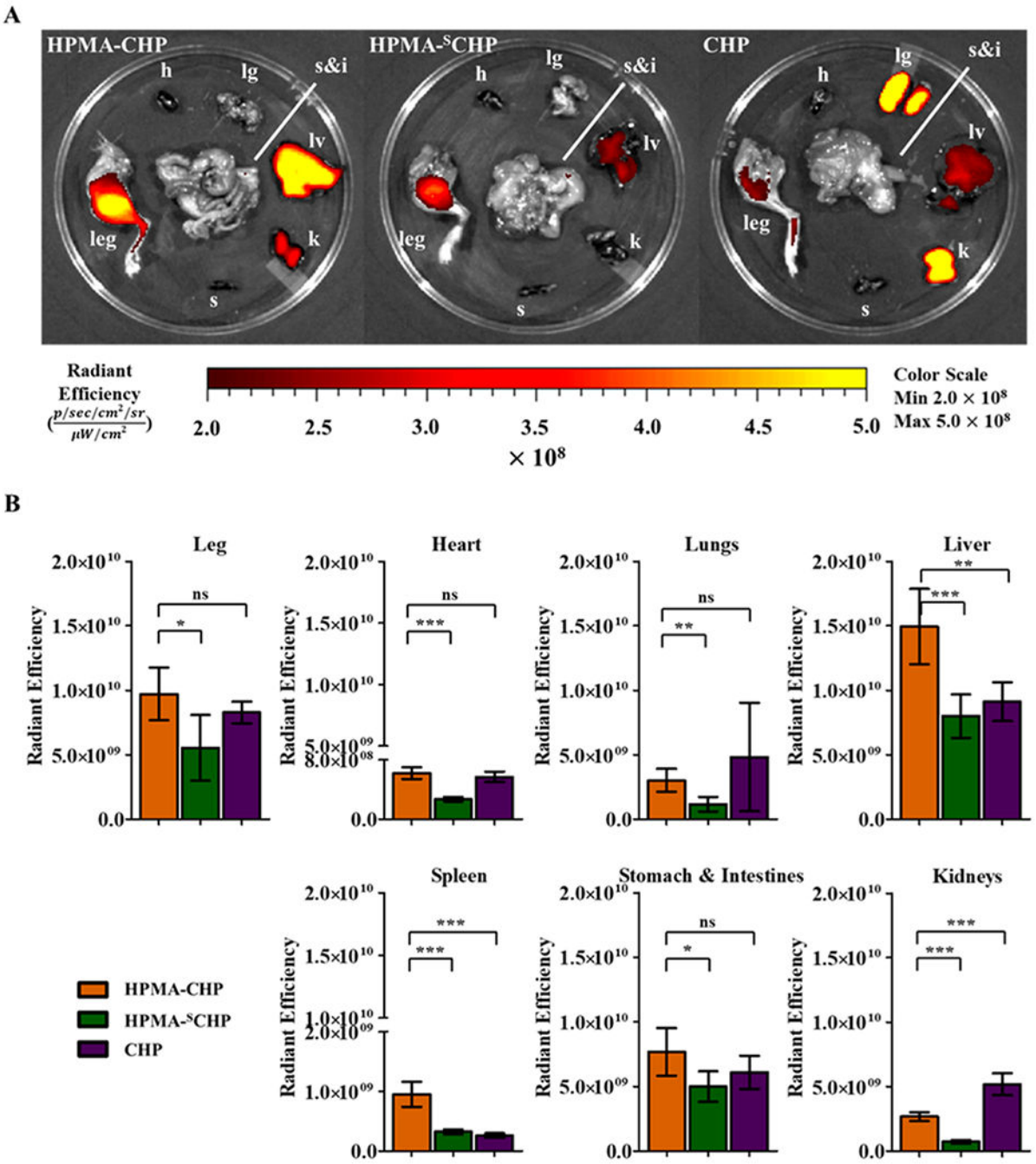

Figure 5.

(A) Fluorescence images of the heart (h), lung (lg), liver (lv), kidney (k), spleen (s), stomach and intestines (s&i), and tumor-bearing leg (leg) harvested at 168 h from tumor-bearing NSG mice implanted with Saos-2 cells in the right proximal tibia and administered with Cy5.5-labeled HPMA–CHP, HPMA–^{S}CHP, and CHP via tail vein injection; (B) comparison of radiant efficiency at each organ and right leg of the three compounds (mean ± SD, $N = 6$, $^{*}p < 0.05$, $^{**}p < 0.01$, $^{***}p < 0.001$).

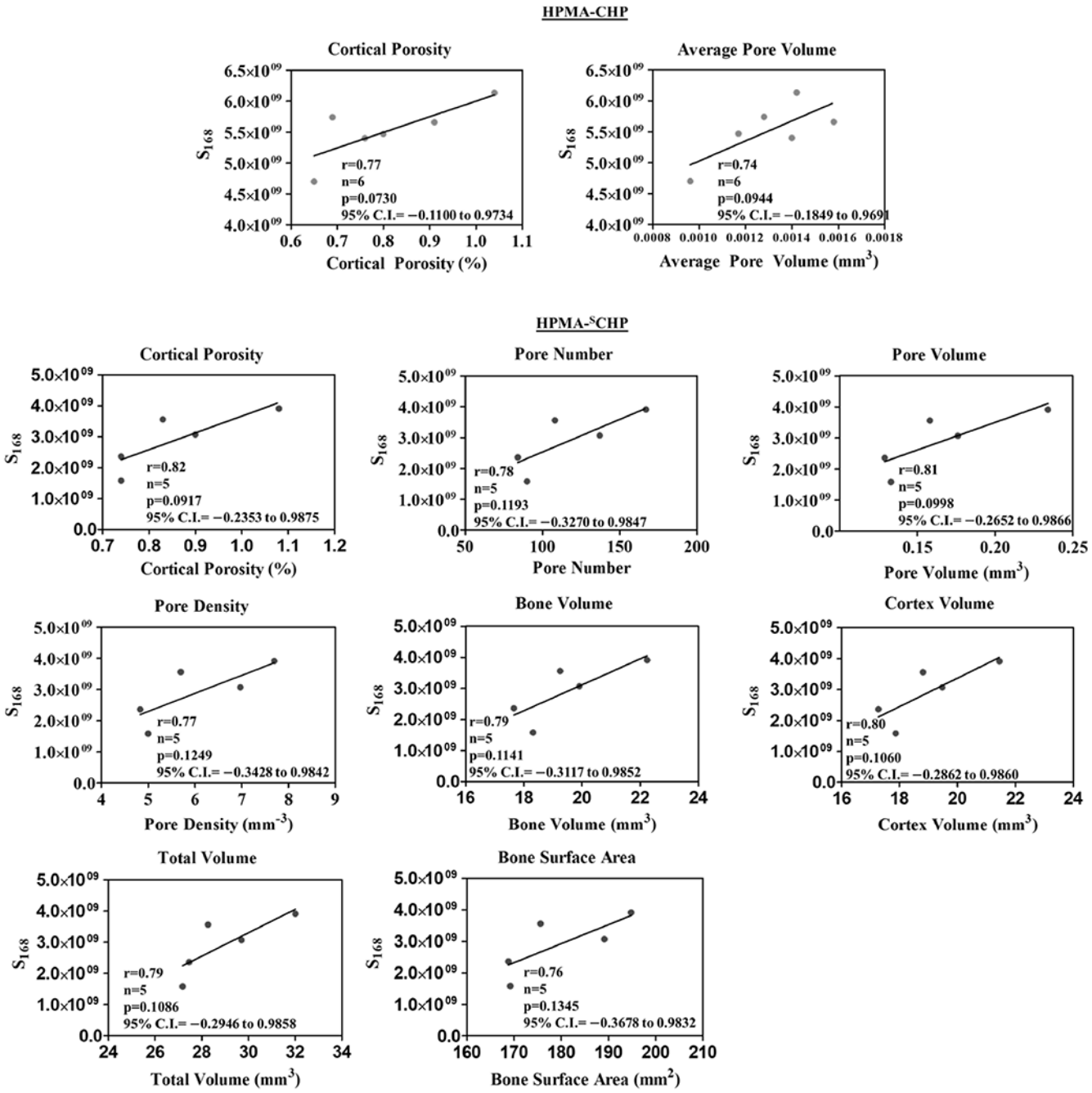

Figure 6.

Correlation of cortical porosity, bone volume, and bone surface area parameters extracted from μ-CT images against tumor accumulation at 168 h (S_{168}) in radiant efficiency, including Pearson's correlation coefficient (r), sample size (n), p-value (p), and 95% confidence interval (95% CI) for tumor-bearing NSG mice implanted with Saos-2 cells in the right proximal tibia and administered with Cy5.5-labeled HPMA–CHP and HPMA–^{S}CHP via tail vein injection.

Table 1.

Noncompartmental Pharmacokinetic Analysis of HPMA–CHP, HPMA–^{S}CHP, and CHP in Intratibial Osteosarcoma Tumors, with Area under the Curve (AUC), Maximum Accumulation (S_{max}), Time to Maximum Accumulation (t_{max}), Tumor Half-Life ($t_{1/2}$), and the Ratio of Accumulation at 168 h to Maximum Accumulation (S_{168}/S_{max})[a]

	HPMA–CHP	HPMA–^{S}CHP	CHP
AUC (rad eff × h)	1.8×10^{12}	1.1×10^{12}	1.5×10^{12}
S_{max} (rad eff)	1.9×10^{10}	1.1×10^{10}	2.3×10^{10}
t_{max} (h)	6	24	6
t1/2 (h)	97.9	77.8	67.5
S_{168}/S_{max}	0.29	0.27	0.16

[a]Parameters are determined using quantification of radiant efficiency (rad eff) from IVIS fluorescence imaging.